Experimental study on turbulent flame speed scaling of expanding premixed flames

Tao Shu,[1] Yuan Xue,[1] Abhishek Saha,[2] Jialong Huo,[1] Hua Zhou,[3]
Zhuyin Ren,[3,*] and Chung K. Law[1,4]
[1]*Center for Combustion Energy, Tsinghua University, Beijing 100084, China*
[2]*Department of Mechanical and Aerospace Engineering, University of California San Diego, La Jolla, California 92093, USA*
[3]*Institute for Aero Engine, Tsinghua University, Beijing 100084, China*
[4]*Department of Mechanical and Aerospace Engineering, Princeton University, Princeton, New Jersey 08544, USA*

(Received 19 July 2022; accepted 22 August 2025; published 22 September 2025)

Characterization of the turbulent flow field in a constant-pressure, dual-chamber, expanding flame apparatus is reported, with the flow field measured by a high-resolution particle image velocimetry system. Eight symmetrically located fans with rotation speed range of 3000 ∼ 7000 rpm generate nearly homogeneous and isotropic turbulent flow with fluctuation velocity linearly ranging from 0.70 to 1.77g m/s, and the integral length scale maintaining about 10 mm. The homogeneity and isotropy of turbulence are verified by statistically analyzing the probability density functions of the instantaneous velocity. Turbulent flame speeds for ethylene/air and ammonia/methane/air mixtures were measured over a range of the turbulent Reynolds number ($Re_T = u'R_f/S_u^0\delta_f$) from 29 to 2706, and from 69 to 2560, respectively. An extended turbulent flame speed scaling correlation is proposed, applicable to both the corrugated flame and thin reaction zone regimes. The extended model accounts for the geometry and history effects of the interaction between turbulence and flame propagation. For ethylene/air and ammonia/methane/air turbulent flame speeds, the Mean Absolute Percentage Error between the experimental and predicted values is 7.8% and 8.5%, respectively, which shows higher accuracy compared to existing scaling models.

DOI: 10.1103/b58g-tsk7

I. INTRODUCTION

The turbulent flame speed, S_T, representing the average rate of propagation of a flame brush through a premixed unburnt gas mixture in a turbulent flow, is an important physical quantity [1] which not only determines the burning rate and combustion efficiency of the flame, but it also affects the flame stabilization as well as flashback and blow-out propensities. Consequently, accurate representation of the turbulent flame speed based on scaling laws is a subject of active research in premixed turbulent combustion. Specifically, there have been extensive studies on hydrocarbon fuels concerning the scaling correlations between the turbulent flame speed and the parameters that describe the properties of fuels and the flow field [2–12]. The earliest scaling theory was that of Damköhler [2], which indicates that the turbulent flame speed is enhanced by large-scale vortices that increase the flame surface, and small-scale vortices that increase the mass and thermal diffusive transport in the flame preheat zone. Based on the above concept, extensive studies have

*Contact author: Zhuyinren@tsinghua.edu.cn

been proposed that correlate the turbulent flame speed with the characteristics of laminar combustion such as the laminar flame speed (S_u^0), the flame thickness (δ_f), the Lewis number (Le) defined as the ratio between the heat and mass difussivities, the Markstein number (Ma), the normalized pressure (P/P_0); and with the turbulence characteristics such as the fluctuation velocity (u'), the integral length scale (l_T), and the Reynolds number (Re). Lu *et al.* [13] investigated stretch effects on the turbulent flame speed using direct numerical simulation of statistically planar turbulent premixed flames, showing that the stretch factor affects the turbulent burning velocity and flame surface area, especially at elevated pressures. It is also found that, for statistically planar flames, stretch effects are significant only for Le smaller than unity, such as lean hydrogen/air and rich heavy hydrocarbons/air flames.

To determine the most appropriate correlations that can be utilized under various conditions, Burke *et al.* [14] compared 16 turbulent flame speed correlations for several hydrocarbon fuels (methane, ethane, and propane) at elevated pressures. Results showed that the smallest mean absolute percentage error (MAPE) among these correlations is still more than 30%, and the correlation with the smallest MAPE cannot be applied universally covering most conditions.

Studies have indicated that the thickness, wrinkling, and evolution of the turbulent flame brush are dependent on both geometry and history, being strongly influenced by the topology of large-scale motion [8,15,16]. Specifically, the degree of wrinkling at any given streamwise location is affected by the history of wrinkling at upstream positions. Consequently, the idealized "geometry independent" correlations given by previous studies may need adjustments for cases where the flame has not fully developed or where the effects of initial geometry-dependent large-scale motion remain. For instance, a Bunsen flame stabilized over a large-diameter burner, which has a greater distance for wrinkling to develop, will exhibit more pronounced wrinkling compared to a shorter flame stabilized over a small-diameter burner. Therefore, the burner size W, or the normalized size, W/l_T, should be an additional parameter to account for the geometry effects [8].

As for turbulent expanding flames, the wrinkling process and turbulent flame brush are also affected by the geometry and history effects during the early stage of flame development. Many existing scaling laws for turbulent expanding flames such as the one by Chaudhuri *et al.* [17] are mainly based on the analysis of the flame surface wrinkling process, and the accuracy of the above models is still subject to further improvement, particularly for $Le < 1$ mixtures. The scaling proposed [17], $S_T/S_u^0 \sim Re_T^{1/2}$, considers the increase in flame surface area due to flame surface wrinkling under the action of turbulent eddies. In this scaling, the flame based turbulent Reynolds number, $Re_T = u'R_f/S_u^0\delta_f$, includes the normalized hydrodynamic length scale R_f/δ_f, and the normalized development time $t/(\delta_f/u')$ and is introduced to account for the geometry and history effects in flame propagation, respectively. Note that the experimental data for scaling analysis is often quite limited, with the mean flame radius being up to about 3.5 cm. Within this range, the flame radius is of the same order as the integral length scale (about 1.0 cm in the experimental apparatus). The geometry and history effects may be significant for the scaling law applicable to this early stage of expanding flame development.

The present experimental study has utilized ethylene/air and ammonia/methane/air turbulent expanding flames, yielding data for scaling analysis and model verification. Here we note that ammonia/methane/air blending mixtures hold the potential as being low carbon emission [18–20], while ethylene (C_2H_4) is a main cracking and decomposition intermediate in the oxidation of alkanes and alkenes, and plays an important role in the combustion of practical fuels such as diesel and aviation kerosene [21]. Because of the practical importance of ethylene, there have been substantial studies of ethylene flame properties [22–25] by simulations and experiments [26–28]. However, the experimental turbulent flame speed data of ethylene/air flames with high fidelity, especially in homogeneous and isotropic turbulent flows under constant pressure, are quite limited.

We also note that the interaction between the turbulent flow and the flame front varies in different regimes of turbulence intensities and flame speeds. With the constant-pressure expanding flame apparatus, and with ethylene as a representative hydrocarbon fuel, turbulent flames mainly in the corrugated flame regime are studied. For ammonia/methane/air mixtures, turbulent flames in the thin reaction zone regime are generated due to their lower burning velocity and thicker flame structure. Thus, the scaling correlation from the experiment data of two substantially different fuels covering both the corrugated flame regime and the thin reaction zone regime incorporate both fundamental and practical importance.

The paper is organized into five sections. The experimental setup of turbulence characterization and flame speed measurement is described in Sec. II. Then, the analysis of nearly homogeneous and isotropic turbulent flow and flame regimes is presented in Sec. III. In Sec. IV, the effects of turbulence intensity, pressure, and fuel properties on turbulent flame propagation are analyzed. In addition, an extended scaling correlation is proposed accounting for geometry and history effects in the flame propagation. The extended correlation is verified utilizing the experimental data of ethylene/air and ammonia/methane/air turbulent expanding flames. Concluding remarks are given in Sec. V.

II. EXPERIMENTAL METHODOLOGY

The experiments of turbulence calibration and flame speed measurement were conducted in a constant-pressure, dual-chamber, expanding flame apparatus, reported in Ref. [25,29,30]. The apparatus consists of two concentric chambers, a cylindrical outer chamber that radially surrounds a spherical inner chamber. The outer chamber (560-mm internal diameter and 410-mm length) is initially filled with an inert gas to balance the pressure in the inner chamber. The spherical inner chamber has a diameter of 250 mm (total volume of 8.18 L), and is initially filled with the combustible premixed gas for testing. This configuration ensures a sufficiently long flame evolution period, minimizing the influence of both initial stochastic disturbances and wall effects. The fuel/air mixtures are ignited by a spark needle positioned at the center of the inner chamber. Turbulence is generated by eight fans with a variable rotation speed, with the fans installed symmetrically around the central circumference inside the inner chamber. Each fan has six blades and the external ring has a diameter of 68-mm. Furthermore, 48 small holes around the circumference of the outer ring aim to generate homogeneous and isotropic turbulence. Each fan is driven by an electric motor through a peek axis. The electric motor has a power rating of 1.0 kW, and the rotation speed can be adjusted to generate the turbulence with the required intensity. In the presence of a strong turbulent field generated by fans, the spark gap width and the opposing needle position may experience minor perturbations, introducing random initial disturbances to the flame. However, these disturbances gradually diminish as the flame propagates. Although buoyancy and wall effects become more pronounced over time, their impact remains negligible within the scope of this experimental study. Further details of flame extrapolation can be found in Refs. [29,34].

A. Turbulence calibration

The two-dimensional (2D) cold turbulent flow field in the central plane of the inner chamber was calibrated by time-resolved, high-speed, particle image velocimetry (PIV) at various turbulence intensities and elevated pressures. The PIV consists of a double-head Nd: YLF laser manufactured by Litron Lasers. The original beams at wavelength 1053 nm is converted to green 527 nm by frequency doubling. The maximum output power of each beam is 150 W. The circular beams emanating from the laser heads are converted to a thin laser sheets using a set of cylindrical lenses, positioned close to the optical window of the chamber depending on the focal length. This arrangement results in a diverging planar laser sheet which covers a 60 mm × 60 mm area located at the center of the inner chamber. For the PIV, droplets of bis (2-ethylhexyl) sebacate ($C_{26}H_{50}O_4$) generated by an in-house designed jet nebulizer are used. The jet nebulizer is connected between the supply line of the (inert gas) nitrogen to the inner chamber, and as such the droplets are added while filling the gas. The average diameter of the seeding particles (droplets) is around 1–2 μm, which is small enough to follow the flow properly but large enough to provide good scattering of the 527-nm green laser.

A high-speed camera, Photron SA-Z is used in the double exposure mode to obtain the correlated image-pairs with a 100-μs interval between them. This ensured that the minimum displacement of the particles between two successive images is around $4 \sim 5$ pixels on average. The resolution of the Mie scattering image is 62.2 μm/pixel. For each rotational speed of the fan, 500 pairs of images are acquired to ensure validity of the statistical data processing. The image pairs are recorded at a rate of 4 kHz which enables 13.1 mJ (70% of the maximal power) energy per pulse. The total time of one test is 0.125 s, which contains about a dozen turnover times at the integral length scale (as presented in Sec. III, the integral length scale is about 10 mm, with the turnover time of 0.01 s). The autocorrelation of the particle image pairs is analyzed by the DaVis Imaging Software from LaVision. The image size is 63.7×63.7 mm. The specific filter length for sliding average is eight pixels to determine background value to subtract and the particle intensity normalization is four pixels. The image is interpreted by cross correlation. A sophisticated adaptive multipass method is selected to reduce the cell size with 32×32 interrogation window size in No. 2 passe and 16×16 interrogation window size in NO. 3 passe. Overlap of the two adjacent interrogation windows is 50%.

B. Flame speed measurement

The two chambers are initially separated by four groups of switch valves with holes that are off-set from each other. The combustible mixtures are added into the inner chamber based on the partial pressure of each species, while the outer chamber is filled with an inert gas (usually nitrogen) at the same pressure. The pressure difference between the inner and outer chambers is measured by a differential pressure transducer to ensure that it stays small. Before ignition, the turbulence-generating fans are run to generate nearly homogenous and isotropic turbulent flows. Then, the combustible mixture is ignited by a centrally located electrode as soon as the switch valves are opened and the inner and outer chambers connected. The motors are kept on during the entire flame propagation duration. The diameter of the electrodes is 0.5 mm, and the spark gap between the two electrodes are set to 0.5 and 2.0 mm for the ethylene/air and ammonia/methane/air flames, respectively. For the ethylene/air flame, the electrostatic energy is stored in an electric capacitor of 200 μF, with the voltage of 100 V. For ammonia/methane/air flame, the electrostatic energy is stored in an electric capacitor of 470 μF with the voltage of 120 V due to the higher ignition energy required.

For optical access, Schlieren images of flame propagation are recorded by a high-speed camera (Photron Fastcam SA-Z). Images are taken at $4000 \sim 20\,000$ frames per second (fps) with 1024×1024 pixels, and hence the spatial resolution is roughly 0.2 mm/pixel. Typical Schlieren images of ethylene/air turbulent expanding flames at different conditions are shown in Fig. 1. It is seen that the outer edge of the flame is visible due to the sharp density gradient at the surface. The flame radius is defined as $R_f = \sqrt{A_f/\pi}$ with A_f being the flame sectional area of the image, which defines an average value of the flame radius. Then, the turbulent flame speed is calculated as

$$S_T = (dR_f/dt)/\theta,$$

which defines a global-average propagation speed. Thermal expansion is defined as $\theta = \rho_u/\rho_b$. The fronts of the turbulent flame are strongly wrinkled even at small flame radius, which indicates that the dynamics of the turbulent flame is mainly controlled by the flow instead of the intrinsic instability of the flame. Our experiments with laminar flames and other experiment results [31–33] show that these conditions are not affected by instabilities. Increasing the rotation speed results in more wrinkling due to the increased turbulence intensity. Meanwhile, higher pressure leads to a thinner local flame structure, hence more wrinkling, which increases the flame-front surface and hence the global flame propagation speed.

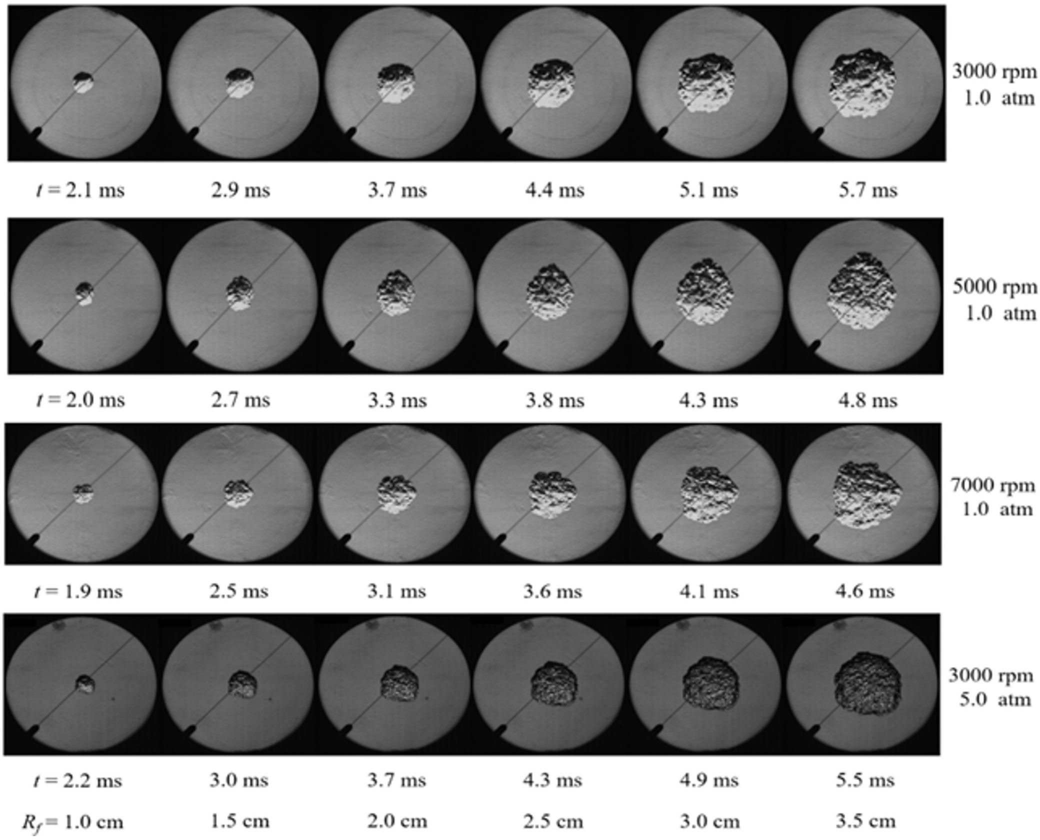

FIG. 1. Typical Schlieren images of expanding ethylene/air turbulent flames. $\phi = 1.0$, $T_u = 298\ K$.

The experimental conditions are summarized in Tables I and II for ethylene/air and ammonia/methane/air flames, respectively. The unburnt temperature of the mixtures, T_u, is 298 K, and the variations of the temperature are kept within ± 3 K. The component concentrations are calculated according to the formula:

$$\phi C_2H_4 + 3(O_2 + 3.762N_2),$$

$$\phi[\alpha CH_4 + (1-\alpha)NH_3] + [2\alpha + 0.75(1-\alpha)](O_2 + 3.762N_2),$$

for ethylene/air and ammonia/methane/air flames, respectively, where ϕ is the equivalence ratio, and α is the mole fraction of methane in the binary fuel blend.

TABLE I. Experimental conditions for ethylene/air turbulent flames.

Fluctuation velocity (m/s)	P (atm)	ϕ
0.70 (3000 rpm)	0.75, 1.0, 3.0, 5.0	0.6, 0.8, 1.0, 1.2, 1.4, 1.6
1.24 (5000 rpm)	0.75, 1.0, 3.0, 5.0	0.6, 0.8, 1.0, 1.2, 1.4, 1.6
1.77 (7000 rpm)	0.75, 1.0, 3.0, 5.0	0.6, 0.8, 1.0, 1.2, 1.4, 1.6

TABLE II. Experimental conditions for ammonia/methane/air turbulent flames. The ignition at $P = 1.0$ atm, $\alpha = 0.3$, $u' = 1.77\,\text{m/s}$, $\phi = 1.2$ failed.

P (atm)	α (CH_4)	$u' = 0.70\,\text{m/s}$ ϕ (3000 rpm)	$u' = 1.24\,\text{m/s}$ ϕ (5000 rpm)	$u' = 1.77\,\text{m/s}$ ϕ (7000 rpm)
1.0	0.3	0.8, 1.0, 1.2	0.8, 1.0, 1.2	0.8, 1.0
	0.5, 0.7	0.8, 1.0, 1.2	0.8, 1.0, 1.2	0.8, 1.0, 1.2
3.0	0.3, 0.5, 0.7	1.0	1.0	1.0
5.0	0.3, 0.7	1.0	1.0	1.0
	0.5	0.8, 1.0, 1.2	0.8, 1.0, 1.2	0.8, 1.0, 1.2

III. CHARACTERIZATION OF TURBULENT FLOW AND FLAME

A. Flow analysis

The PIV analysis provides the instantaneous 2D velocity filed, $u(x, y)$. For convenience, the horizontal and vertical components of $u(x, y)$ are labeled as $U(x, y)$ and $V(x, y)$ in the two orthogonal directions, respectively. By averaging the instantaneous velocity of 500 vector maps, the time-average velocity components in the two orthogonal directions, i.e., $\bar{U}(x, y)$ and $\bar{V}(x, y)$ can be determined. Then, the root mean square (RMS) of the component velocity fluctuations, i.e., $U_{RMS}(x, y)$ and $V_{RMS}(x, y)$, can be calculated by subtracting the mean velocities from the instantaneous ones. The resultant fluctuation velocity, labeled as u', is the root mean square of $U_{RMS}(x, y)$ and $V_{RMS}(x, y)$, measuring the turbulence intensity. To measure the correlation of the two orthogonal velocity components, the velocity covariance is calculated as:

$$Cov_{uv}(x_i, y_i) = \frac{1}{n}\sum_{j=1}^{n}[U(x_i, y_i) - \bar{U}(x_i, y_i)][V(x_i, y_i) - \bar{V}(x_i, y_i)]. \tag{1}$$

Since the flame is ignited at the center of the inner chamber, resulting in a turbulent expanding flame propagating outwardly from the center to the wall, the circular mean velocity covariance and the RMS velocity are also identified according to the following relations:

$$Cov_{uv} = \left[\frac{1}{N}\sum_{j}^{N} Cov_{uv\,j}\right]_{\text{circle}}, \tag{2}$$

$$U_{RMS} = \left[\sqrt{\frac{1}{N}\sum_{j}^{N} {U'_j}^2}\right]_{\text{circle}}, \tag{3}$$

$$V_{RMS} = \left[\sqrt{\frac{1}{N}\sum_{j}^{N} {V'_j}^2}\right]_{\text{circle}}. \tag{4}$$

Note that the mean covariance is the arithmetic average, and the region of the concentric rings is from 0 to 30 mm with a radius interval of 1.5 mm.

As shown in Fig. 2(a), from the center of the chamber towards the wall, the mean velocity covariance almost keeps unchanged and remains at low values close to zero. With increasing fan rotation speed, the mean velocity covariance shows a slight deviation from zero but still keeps at low values even at the rotation speed of 7000 rpm. Figure 2(b) shows the RMS and fluctuation velocity of the turbulent flow field at different circular regions. The two RMS velocity components both exhibit a nearly constant value at different radii for fixed fan rotation speed. The differences between U_{RMS} and V_{RMS} are no more than 0.2 m/s under nearly all test conditions. With the fan rotation speed

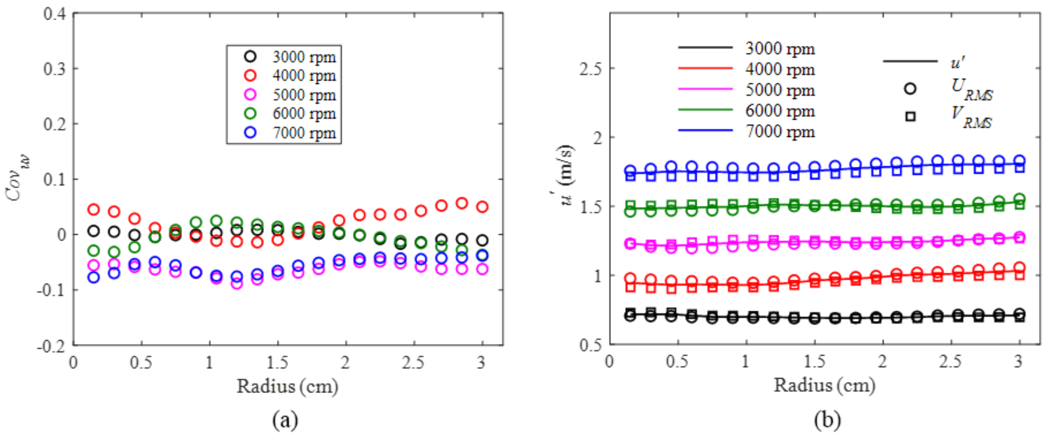

FIG. 2. Velocity statistics in circular mean regions. (a) Circular mean velocity covariances; (b) circular mean RMS and fluctuation velocities.

increasing, the RMS velocity and fluctuation velocity increase monotonically, which indicates that higher rotation speed generates stronger turbulence intensity. This tendency is consistent with what is observed in Refs. [34,35]. Additionally, the PIV flow field calibrations are repeated five times at each condition, and the global statistical quantities such as the circular mean velocity covariance, RMS velocity, fluctuation velocity, integral length, etc. shown in Fig. 2 and the following figures are case averaged. These plots confirm that the turbulence generated by the fans in the 2D plane of measurement is indeed nearly homogenous and isotropic.

Since the fluctuation velocities almost keep at constant values in regions with different radii, the spatial averaged fluctuation velocities in the entire region (6.0 cm × 6.0 cm) at elevated pressures are shown in Fig. 3. It is seen that the fluctuation velocity has strong linearity with the rotation speed of the fans. The fluctuation velocity and rotation speed can be fitted as

$$u' = 2.67 \times 10^{-4} n - 0.10, \tag{5}$$

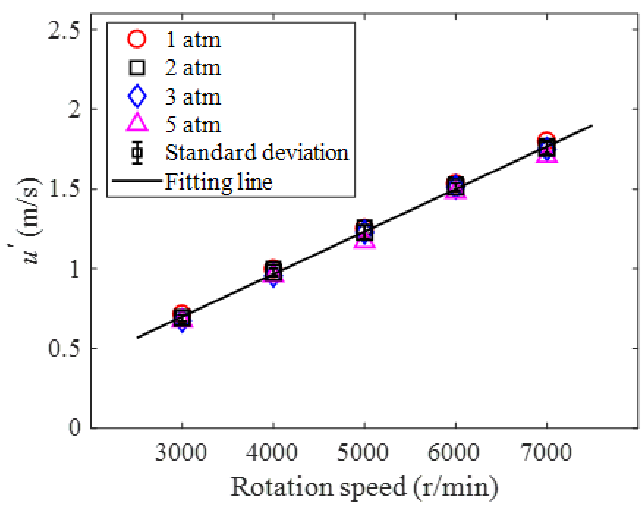

FIG. 3. Correlation between RMS velocities and rotation speeds of fans.

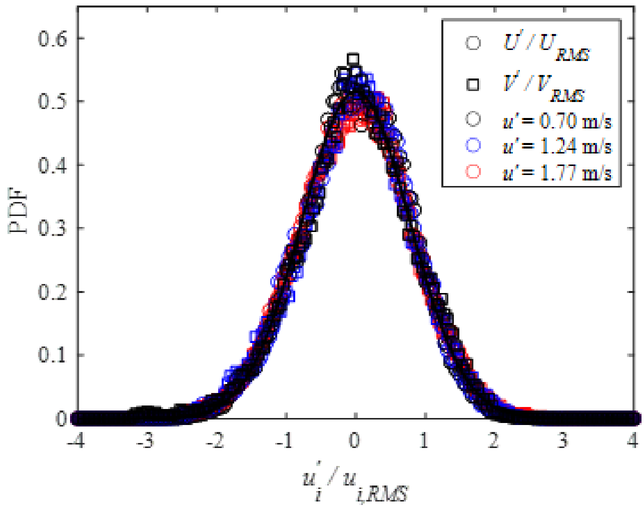

FIG. 4. PDFs of the normalized instantaneous fluctuation velocities. The black line is the Gaussian distribution fitted by data.

where n is the rotation speed of fans with the unit of rpm, and u' has the unit of m/s. The correlation coefficient of the above expression is 0.9996, which indicates strong linearity. For a fixed fan speed, the fluctuation velocity at lower pressures is somewhat larger than that at higher pressures. Moreover, the difference of fluctuation velocity between the low and high pressures increases with increasing fan speed. As for the rotation speed of 7000 rpm, the difference of the fluctuation velocity between 1.0 and 5.0 atm is about 0.1 m/s, which is much smaller than the fluctuation velocity at this rotation speed. Thus, the above difference in fluctuation velocity at various pressures is negligible. In the following, the fluctuation velocities at different pressures are taken to be the same value calculated from the above correlation formula, i.e., 0.70, 1.24, 1.77 m/s for the rotation speed of 3000, 5000, 7000 rpm, respectively.

The probability density functions (PDFs) are also utilized to describe the turbulent velocity field. As is shown in the early works of Townsend [36], the velocity PDFs should exhibit symmetry for homogeneous and isotropic turbulent flows. In order to verify this, the PDFs of the instantaneous fluctuation velocity field normalized by the local RMS velocity have been estimated in Fig. 4. To further check the symmetry of the PDFs, higher-order standardized moments, namely the skewness factor (S_k), is also calculated, noting that the skewness factor is the third moment of the fluctuation velocity normalized by the corresponding RMS velocity component, characterizing the asymmetry of the distribution such that a perfectly symmetrical PDF would lead to a zeroth skewness factor. For $S_k > 0$, it is more likely to result in larger positive fluctuations than negative ones and the reverse holds for $S_k < 0$. The case-averaged skewness factors, as well as the RMS, fluctuation velocities, and velocity covariances at typical conditions are summarized in Table III. It is seen that the skewness factors are between -0.02 and 0.02 for both the horizontal and vertical velocity components, which are close to zero. As such, the PDFs of the instantaneous fluctuation velocity field can be considered symmetrical. In addition, the Gaussian distribution line fitted by data is also shown in Fig. 4, indicating that the velocity PDFs are close to the Gaussian distribution.

Homogeneity of the turbulence implies that the characteristics of the turbulent flow field are independent of the shift of the coordinate system [37], which quantifies the uniformity of the flow field. It is defined as the ratio between the local RMS velocity and the spatially averaged one. Expression of the homogeneity is given by the following relations for each component of the

TABLE III. RMS, fluctuation velocities, velocity covariances, and skewness factors.

Rotation speed	3000 rpm	5000 rpm	7000 rpm
U_{RMS} (m/s)	0.69	1.23	1.80
V_{RMS} (m/s)	0.70	1.25	1.73
u' (m/s)	0.70	1.24	1.77
u_{xy} (m^2/s^2)	0.00	−0.06	−0.18
$S_{k,U}$	−0.02	−0.02	0.02
$S_{k,V}$	0.02	−0.01	0.01

velocity:

$$H_U(x_i, y_i) = U_{RMS}(x_i, y_i)/\overline{U}_{RMS}, \tag{6}$$

$$H_V(x_i, y_i) = V_{RMS}(x_i, y_i)/\overline{V}_{RMS}. \tag{7}$$

The isotropy of turbulence is also a desired feature that indicates the statistical invariance of the flow field to rotation and reflections of the coordinate system. It should be identical in all directions. The isotropy (I) is estimated from the ratio of the local RMS values in the two perpendicular directions and is given by

$$I(x_i, y_i) = U_{RMS}(x_i, y_i)/V_{RMS}(x_i, y_i). \tag{8}$$

The PDFs of homogeneity and isotropy at typical conditions are shown in Fig. 5, indicating that they are within ±20%. As for a perfectly homogeneous and isotropic turbulent flow, all the above ratios should be unity, and can be fully described by a single RMS intensity value, i.e., fluctuation velocity, which is representative of all velocity components as well as their spatial variations. For an expanding turbulent flame, this simplification translates to perturbation of the expanding flame by external disturbances acting uniformly and equally in all directions.

The integral length scales in the horizontal and vertical directions are determined by integrating the autocorrelation of the corresponding velocity components from the origin to infinity. To utilize the data range as wide as possible, the estimation is performed at the boundary of each direction, i.e.,

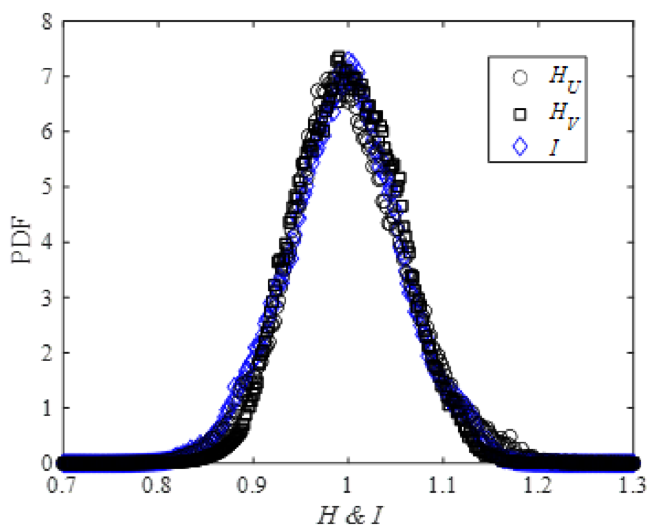

FIG. 5. PDFs of homogeneity and isotropy. $u' = 0.70$ m/s, $P = 1.0$ atm.

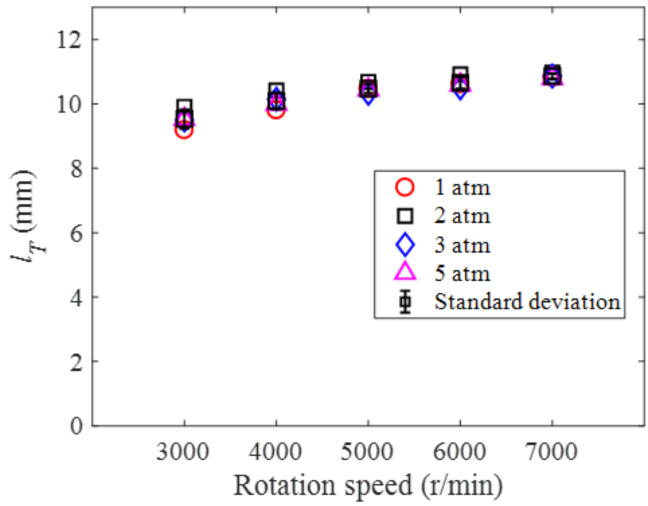

FIG. 6. Integral length scales vs rotation speeds of fans.

from (−3 cm, 0) to (3 cm, 0) for the horizontal direction and from (0, −3 cm) to (0, 3 cm) for the vertical direction, with a total length of 6.0 cm. The integral length scales for the rotation speed from 3000 to 7000 rpm at elevated pressures are shown in Fig. 6. It is seen that the integral length scale increases slowly with increasing rotation speed, being around 10 mm, and is almost independent of pressure. In the following, the integral length scales at different pressures are taken as the mean value calculated at each rotation speed, i.e., 9.6, 10.4, 10.9 mm for 3000, 5000, 7000 rpm, respectively. With the energy cascade concept, based on the Kolmogorov's postulate, there exists a range of scales through which the energy transfer rate is independent of the molecular viscosity. Within this inertial subrange, the dependence of turbulent kinetic energy on the eddy size can be represented by the energy spectrum of $E(k) \sim k^{-5/3}$ with k being the wave number with dimension m^{-1}, according to the "−5/3 law". Examples of the turbulent energy spectrum are shown in Fig. 7 in logarithmic coordinates, demonstrating that the experimental data agree well with the black solid reference line with the slope of $-5/3$.

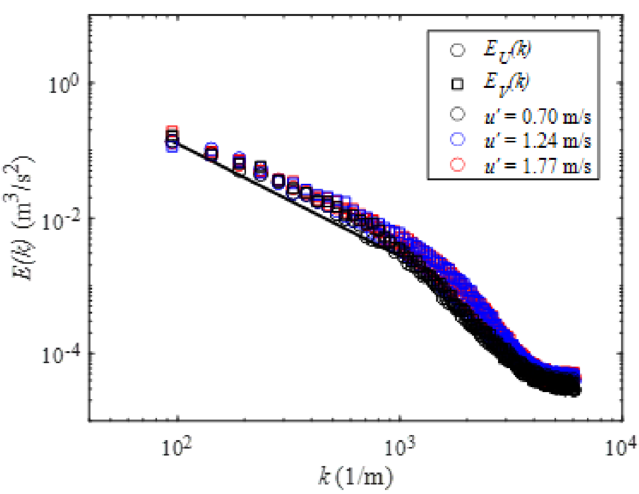

FIG. 7. Schematic of the turbulent kinetic energy spectrum.

TABLE IV. S_u^0 and δ_f of ethylene/air premixed flame.

Equivalence ratio (ϕ)		0.6	0.8	1.0	1.2	1.4	1.6
S_u^0 (cm/s)	0.75 atm	27.2	50.3	64.1	65.8	44.6	26.7
	1.0 atm	25.1	47.6	61.2	62.9	51.3	34.3
	3.0 atm	17.9	36.9	48.9	50.5	39.5	25.7
	5.0 atm	14.8	32.1	43.2	44.3	33.7	21.9
δ_f (mm)	0.75 atm	0.623	0.424	0.370	0.359	0.477	0.724
	1.0 atm	0.498	0.333	0.290	0.280	0.320	0.442
	3.0 atm	0.220	0.135	0.115	0.110	0.130	0.188
	5.0 atm	0.154	0.091	0.076	0.073	0.090	0.130

Summarizing the above analysis, with the spherical vessel equipped with eight symmetrically located fans, it is possible to generate a nearly homogeneous and isotropic turbulent flow at a central 60 mm $\times$ 60 mm planar region within the inner chamber.

B. Regime analysis

Based on the velocity ratio (u'/S_u^0) and the length scale ratio (l_T/δ_f), turbulent combustion is distinguished into different regimes, namely wrinkled flame regime, corrugated flame regime, thin reaction zone regime, and distributed reaction zone regime. The laminar flame speeds (S_u^0) and flame thicknesses ($\delta_f = D/s_L$, where D is the thermal diffusivity) of ethylene/air and ammonia/methane/air mixtures in the above ratios are calculated from 1D freely propagating flame simulations. The detailed mechanism USC-Mech II [38], that has been verified with relatively high accuracy at 0.75 $\sim$ 10 atm by Huo *et al.* [25], is utilized in the calculation of ethylene/air flames. Also, the detailed mechanism of Okafor *et al.* [18], which has been verified in Ref. [30], is utilized for the ammonia/methane/air flames. The laminar flame speed and flame thickness for scaling analysis are summarized in Tables IV and V for ethylene/air and ammonia/methane/air flames, respectively.

TABLE V. S_u^0 and δ_f of ammonia/methane/air premixed flame.

	Methane content (α)	$\alpha = 0.3$	$\alpha = 0.5$	$\alpha = 0.7$
S_u^0 (cm/s)	$P = 1.0$ atm, $\phi = 0.8$	9.76	14.0	18.5
	$P = 1.0$ atm, $\phi = 1.0$	14.1	19.5	25.3
	$P = 1.0$ atm, $\phi = 1.2$	11.7	15.5	20.2
	$P = 3.0$ atm, $\phi = 1.0$	8.93	12.0	15.7
	$P = 5.0$ atm, $\phi = 0.8$	5.71	7.36	8.93
	$P = 5.0$ atm, $\phi = 1.0$	8.82	11.0	13.1
	$P = 5.0$ atm, $\phi = 1.2$	8.22	9.30	10.3
δ_f (mm)	$P = 1.0$ atm, $\phi = 0.8$	1.27	0.917	0.723
	$P = 1.0$ atm, $\phi = 1.0$	1.02	0.763	0.609
	$P = 1.0$ atm, $\phi = 1.2$	1.24	0.939	0.725
	$P = 3.0$ atm, $\phi = 1.0$	0.503	0.379	0.297
	$P = 5.0$ atm, $\phi = 0.8$	0.420	0.329	0.272
	$P = 5.0$ atm, $\phi = 1.0$	0.318	0.258	0.216
	$P = 5.0$ atm, $\phi = 1.2$	0.345	0.305	0.272

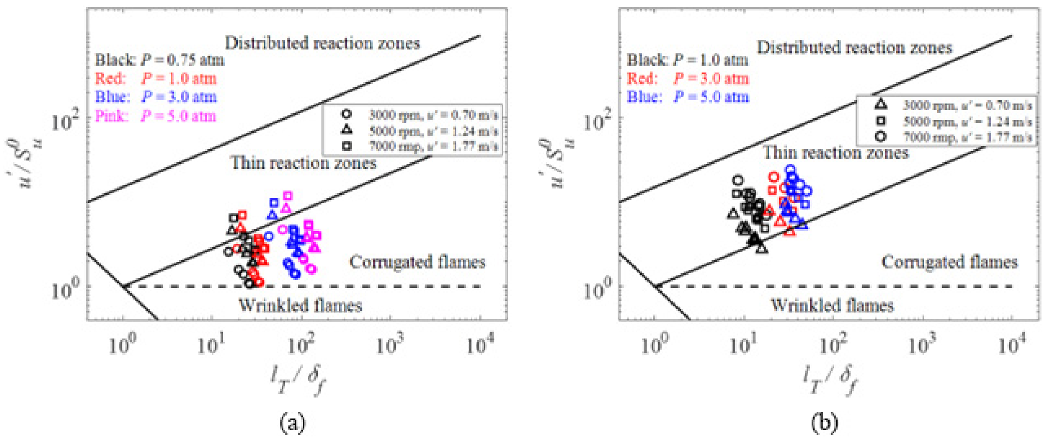

FIG. 8. Turbulent regime diagram for expanding flames. (a) Ethylene/air flames; (b) Ammonia/methane/air flames.

Figure 8 presents the experimental conditions for ethylene/air and ammonia/methane/air flames within the regime diagram. The experimental cases for ethylene/air flames span both the corrugated flame and thin reaction zone regimes, whereas nearly all ammonia/methane/air flame cases fall within the thin reaction zone regime, primarily due to their lower laminar flame speeds and greater flame thickness. In the corrugated flame regime, the interaction between turbulence and the flame results predominantly from flame surface wrinkling. In contrast, in the thin reaction zone regime, the interaction is influenced by both the wrinkling of the flame surface caused by large-scale vortices and the enhancement of mass and heat transfer in the preheat zone by small-scale vortices

IV. ANALYSIS OF TURBULENT FLAME SPEED

A. Turbulent flame speeds of ethylene/air and ammonia/methane/air mixtures

Figure 9 shows variations of the turbulent flame speeds of ethylene/air mixtures at different operating conditions. For the reference condition of $P = 1$ atm, $\phi = 1$, and $u' = 0.70$ m/s, the dependence of the normalized turbulent flame speed, relative to the laminar flame speed, on the fluctuation velocity, pressure, and equivalence ratio is analyzed. In general, a large fluctuation velocity increases flame wrinkling and hence the flame surface density, which in turn increases the turbulent flame speed.

In addition, as shown in Figs. 9(a) and 9(c), the normalized turbulent flame speeds at various equivalence ratios are almost the same at low turbulence intensity ($u' = 0.70$ m/s) under normal pressure. As turbulence intensity increases ($u' = 1.77$ m/s), the normalized turbulent flame speed becomes more sensitive to fluctuation velocity, particularly under highly rich or lean conditions. As shown in Fig. 9(b), for a fixed fluctuation velocity, normalized turbulent flame speeds at higher pressures are greater than those at lower pressures, hence suggesting that in the wrinkled and corrugated flame regimes, the flame surface density increases with elevated pressure resulting from reduced flame thickness and subsequent stronger surface wrinkling by vortices. The effect is more pronounced especially for the large fluctuation velocity of 1.77 m/s. It is important to note that since the above results are appropriately considered on the basis of the normalized turbulent flame speed, which is the ratio of the turbulent flame speed to the laminar flame speed, the direct influence of density and hence pressure through the definition of burning rate, which is the product of density and flame speed, is cancelled out. For rich hydrocarbon/air mixtures, the flame thickness and flame speed are more significantly affected by hydrodynamic and diffusional-thermal instabilities, which diminish the impact of turbulence-driven enhancement. Our previous studies [39] have shown

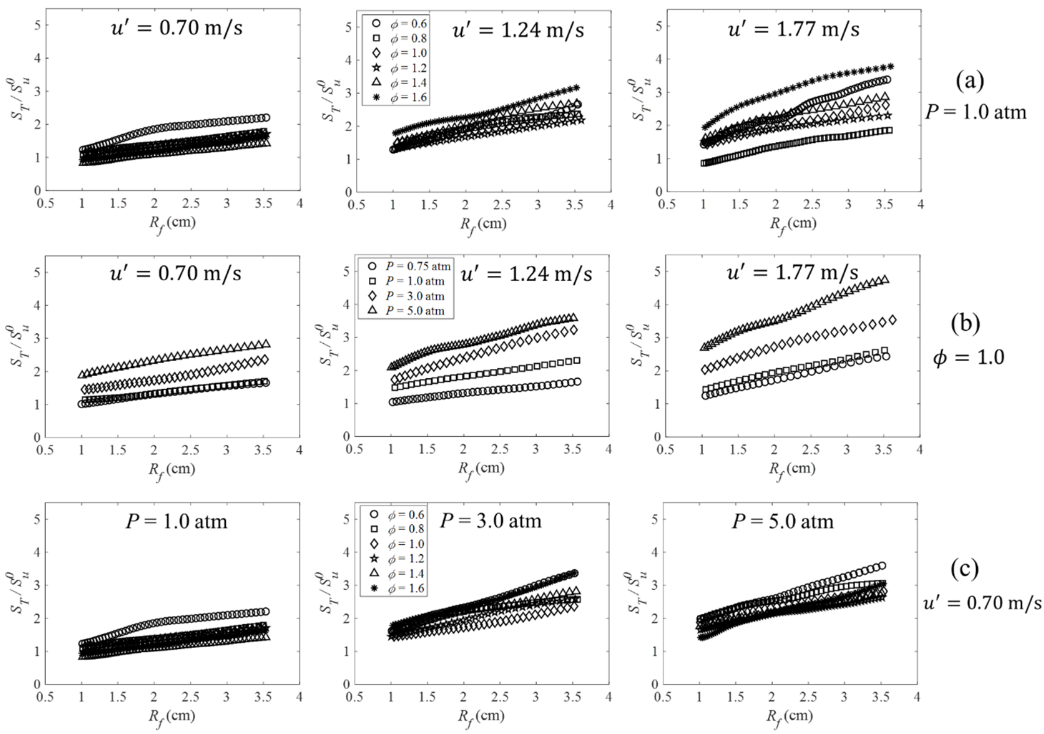

FIG. 9. Ethylene/air turbulent flame speeds varying with the flame radii. Only one realization is shown for a set of given pressure, fluctuation velocity, and equivalence ratio. (a) $P = 1.0$ atm, $u' = 0.70 \sim 1.77$ m/s, $\phi = 0.6 \sim 1.6$; (b) $P = 0.75 \sim 5.0$ atm, $u' = 0.70 \sim 1.77$ m/s, $\phi = 1.0$; (c) $P = 1.0 \sim 3.0$ atm, $u' = 0.70$ m/s, $\phi = 0.6 \sim 1.6$.

that the measured critical flame radii for the onset of the transition and global pulsation stages decrease with increasing pressure and decreasing equivalence ratio. However, the nondimensional values, normalized by flame thickness, remain nearly constant across all pressures during the self-acceleration and global pulsation phenomena in the propagation of expanding spherical laminar flames with flame-front instabilities.

Similar observations are made on the dependence of the normalized turbulent flame speeds of ammonia/methane/air mixtures on the fluctuation velocity, pressure, and equivalence ratio, as shown in Fig. 10. In addition, with the variety of methane content for mixtures at the same equivalence ratio, normalized turbulent flame speeds keep almost the same at low turbulent intensity ($u' = 0.70$ m/s) under normal pressure. With increasing turbulent intensity, the difference of normalized turbulent flame speed for the mixture with different methane content is prominent.

The enhancement of turbulent flame speed due to the flame-turbulence interaction is often characterized by the Reynolds number, defined as

$$Re = UL/\nu, \tag{9}$$

where the characteristic velocity and length scale are the fluctuation velocity (u') and the integral length scale (l_T), respectively. Taking the kinematic viscosity of air at atmospheric pressure as a standard ($\nu = 15.5 \times 10^{-6}$ m^2/s, $T = 298$ K), assuming that the kinematic viscosity is inversely proportional to pressure, the range of the Reynold number in this work is $325 \sim 6224$ and $433 \sim 6224$ for ethylene/air flames and ammonia/methane/air flames, respectively. Since the kinematic viscosity is also proportional to $S_u^0 \delta_f$ of the corresponding laminar flame (assuming constant Schmidt number, defined as the ratio of kinematic viscosity and mass diffusivity), the Reynolds

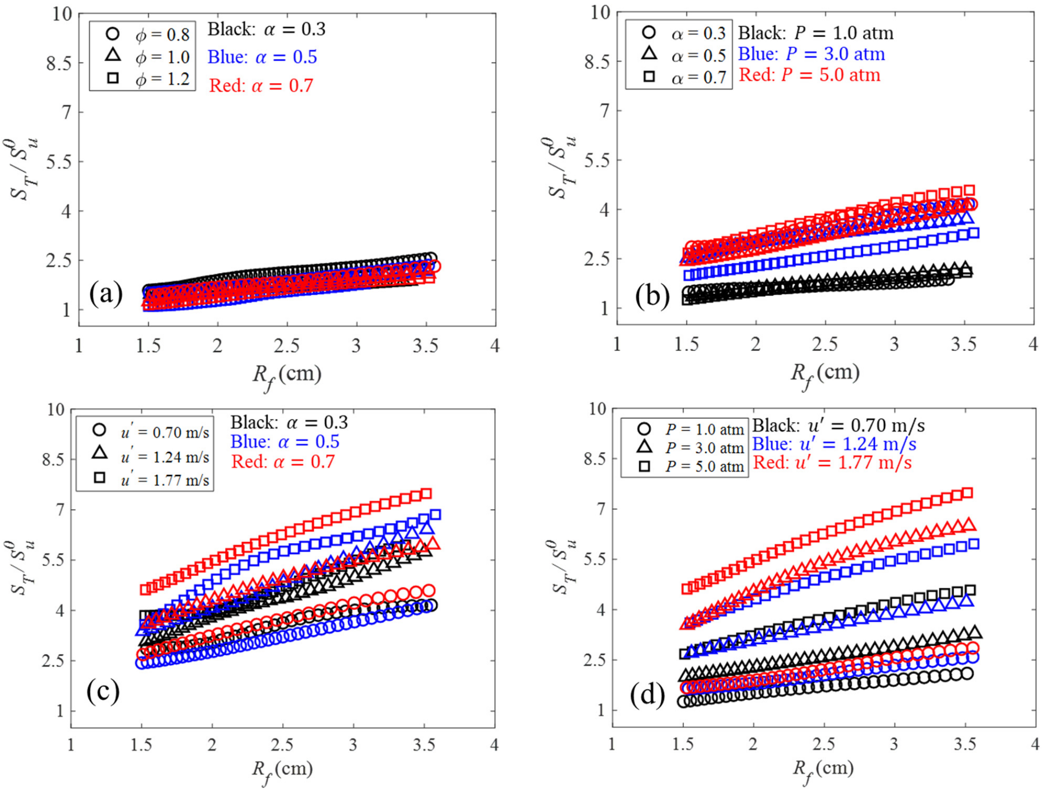

FIG. 10. Ammonia/methane/air turbulent flame speeds varying with the flame radii. Only one realization is shown for a set of given pressure, fluctuation velocity, and equivalence ratio. (a) $P = 1.0$ atm, $u' = 0.70$ m/s; (b) $\phi = 1.0$, $u' = 0.70$ m/s; (c) $\phi = 1.0$, $P = 5.0$ atm; (d) $\phi = 1.0$, $\alpha = 0.7$.

number can also be written as

$$Re_T = u' l_T / S_u^0 \delta_f. \tag{10}$$

As is shown in Eq. (10), a larger fluctuation velocity leads to a larger Reynolds number. Also, higher pressure results in both smaller laminar flame speed and flame thickness and therefore has a larger Reynolds number, given the same fluctuation velocity and integral length scale. In general, turbulent flame speed positively correlates with the Reynolds number, resulting from either wrinkling of the flame surface by large-scale vortices, or both wrinkling of the flame surface by large-scale vortices and strengthening of the thermal and mass transfer by small-scale vortices.

B. Scaling law with geometry and history effects

With the turbulent flame speeds of ethylene/air and ammonia/methane/air flames measured, an extended turbulent flame speed scaling correlation accounting for the geometry and history effect is proposed in this section.

1. *Proposal of the scaling correlation*

As detailed in Sec. III A, flow analysis based on PIV measurements confirms that the turbulence generated by the fans in the measurement zone is nearly homogeneous and isotropic. Under these conditions, the fluctuation velocity *u'* can reasonably be treated as constant. This assumption forms part of the rationale for employing $Ge(t)$ to assess history effects in turbulent flame propagation.

Chaudhuri *et al.* [17,40] proposed that the effect of turbulence on flame propagation can be considered as wrinkling of the flame surface by a multitude of length scales. As is theoretically analyzed in Ref. [40], for the premixed planar and steady flame in a homogeneous and isotropic turbulent flow, given by

$$G(x, y, z, t) = G_0, \tag{11}$$

the normalized turbulent flame speed (S_T/S_u^0) has the leading order of

$$\left(S_T/S_u^0\right) \sim \langle\sqrt{1 + \nabla g \cdot \nabla g}\rangle \sim \left[1 + \int_0^\infty k^2 \Gamma(k) dk\right]^{0.5}, \tag{12}$$

where g, defined as

$$g(x, y, z, t) = G_N - z, \tag{13}$$

is the fluctuating z distance of each $G(x, y, z, t) = G_N$ interface from its corresponding mean position defined as $z = G_N$. Here G_N represents the Nth interface, k is the wave number and $\Gamma(k)$ the g^2 spectrum calculated from the spectral closure of the autocorrelation equation of g. As further analyzed, the integral term is given by

$$\int_0^\infty k^2 \Gamma(k) dk \sim R_f/\delta_f. \tag{14}$$

Consequently, it was suggested [17] that the eddies, which are smaller than the hydrodynamic scale (flame size) of a spherical flame, will wrinkle the flamefront while the larger eddies will only convect the flame. Thus, the effective largest scale of the eddy which wrinkles the flamefront is the hydrodynamic scale, and hence a turbulent Reynolds number is proposed as

$$Re_T = u' R_f / S_u^0 \delta_f, \tag{15}$$

replacing the integral length scale l_T by the flame hydrodynamic length scale R_f. The range of the above turbulent Reynolds number defined by R_f in this work is 29 ∼ 2706 and 69 ∼ 2560 for ethylene/air flame (1.0 cm $\leqslant R_f \leqslant$ 3.5 cm) and ammonia/methane/air flame (1.5 cm $\leqslant R_f \leqslant$ 3.5 cm), respectively. For the current experiments, the integral length scale and the hydrodynamic length scale are of the same order. Combining Eqs. (12), (14), and (15), a turbulent flame speed scaling correlation can be written as

$$S_T/S_u^0 \sim (1 + Re_T)^{0.5}. \tag{16}$$

This correlation has shown the ability to describe turbulent flame propagation in the corrugated flame and the thin reaction zone regimes [17].

In addition, the normalized turbulent flame speed can also be described by

$$S_T/S_u^0 \sim \mathbf{\Sigma} I_0 \delta_T = (\mathbf{\Sigma} \delta_f) I_0 \delta_T / \delta_f, \tag{17}$$

where Σ is the flame surface density, I_0 is the stretch factor, and δ_T is the flame brush thickness [8]. The surface density is defined as the reaction layer surface area per unit volume, with the unit of m^{-1}, which is dominated by the surface wrinkling process and cannot be easily measured in experiments. The term $\Sigma\delta_f$ is the nondimensional surface density normalized by the flame thickness. The brush thickness δ_T has the unit of m, indicating the spatial region where the reaction layers are located. It is shown in Refs. [6,41,42] that the evolution of the brush thickness is self-similar with the hydrodynamic length scale and flame propagation time. The term ($I_0\delta_T/\delta_f$) is the nondimensional stretched brush thickness normalized by the flame thickness. Both the surface wrinkling process and evolution of brush thickness depend on geometry and history effects. Thus, an extended correlation, suggested by the correlations of Eqs. (16) and (17), is proposed, where Eq. (16) describes the essential wrinkling process, and the hydrodynamic length scale and flame propagation time are induced to describe the geometry and history effects on surface wrinkling process and brush thickness evolution.

With the consideration of more general cases, the normalized hydrodynamic length scale (R_f/δ_f) is used to describe the geometry effect. Since the effects of geometry and history also depend on the turbulence intensity, the product of normalized fluctuation velocity (u'/S_u^0) and normalized hydrodynamic length scale (R_f/δ_f), i.e., the turbulent Reynolds number ($Re_T = u'R_f/S_u^0\delta_f$) is eventually adopted to describe the geometry effect. The normalized time $t/(\delta_f/u')$ is adopted to describe the history effect, where t is the flame propagation time and the term δ_f/u' is the eddy turnover time at the scale of flame thickness. Thus, an extended correlation can be written as

$$S_T/S_u^0 \sim Ge(1 + Re_T)^{0.5}, \tag{18}$$

where

$$Ge = {Re_T}^a[1 - \exp(-(\delta_f/u')/t)]^b \tag{19}$$

is a nondimensional prefactor to account for the geometry and history effects. In *Ge*, the normalized time is expressed in the reciprocal form, and the term $[1-\exp(-(\delta_f/u')/t)]$ is approximately unity at the initial stage ($t/(\delta_f/u') \ll 1$) of flame propagation. As the flame expands ($t/(\delta_f/u') \gg 1$), this term approaches $(\delta_f/u')/t$. The time-dependent parameter $Ge(t)$ is introduced to better characterize the entire evolution of turbulent flame propagation, capturing both transient and asymptotic behaviors, explicitly accounts for two physical aspects:

(1) *Geometry effect:* Encapsulated in ${Re_T}^{0.5}$ (where $Re_T = u'R_f/S_u^0\delta_f$), the normalized hydrodynamic length scale (R_f/δ_f) is used to describe the geometry effect. Since the effects of geometry also depend on the turbulence intensity, the product of normalized fluctuation velocity (u'/S_u^0) and normalized hydrodynamic length scale (R_f/δ_f), i.e., the turbulent Reynolds number is eventually adopted to describe the geometry effect.

(2) *History effect:* The exponential decay term $[1-\exp(-\tau/t)]^{0.9}$ ($\tau = \delta_f/u'$) models the relaxation of flame wrinkling from initial conditions toward a statistically steady state. At initial stage, as $t \ll \tau$, *Ge* asymptotically approaches ${Re_T}^{0.5}$. *Ge* approaches a constant value in the final stage with the magnitude of about unity, reducing Eq. (21) to $S_T/S_u^0 \sim 1 + {Re_T}^{0.5}$ (small Re_T) or $S_T/S_u^0 \sim {Re_T}^{0.5}$(large Re_T), which aligns with Damköhler's framework for developed flames. Thus, *Ge* transitions the scaling from initial transients to a steady-state limit, preserving S_{T} as a property of the flame-turbulence system in its asymptotic state.

For practical applications beyond experiments, *Ge* can be simplified as follows:

(1) For developing flames ($t \sim \tau$), *Ge* provides accurate predictions where traditional models fail (MAPE $< 7.8\%$ vs $>18.1\%$ in Table VI).

(2) For fully developed flames ($t \gg \tau$), the scaling law reduces to established models.

Crucially, *Ge* is not an arbitrary fitting parameter but a physics-based correction validated across two distinct fuels (ethylene and ammonia-methane) spanning corrugated and thin-reaction-zone regimes.

2. Determination of the parameters

The MAPE [14] is calculated to determine the parameters *a* and *b*, and also to assess the accuracy of the extended scaling model, which is defined as

$$MAPE = \sum_{i=1}^{N} |(x_{\exp,i} - x_{\mathrm{corr},i})/x_{\exp,i}|/N, \tag{20}$$

where $x_{exp,i}$ is the experimental value, $x_{corr,i}$ the value predicted by the correlation, and N the size of the data. The parameters a and b in the above correlation are fitted separately for ethylene/air and methane/ammonia/air mixtures, where the MAPE has the smallest value within the parameter space. The calibrated result is $a = 0.5$, $b = 0.9$ and $a = 0.5$, $b = 0.91$ (taking the rounding value 0.9) for ethylene/air and methane/ammonia/air mixtures, respectively.

TABLE VI. Turbulent flame speed scaling correlations. $P_0 = 1$ atm is the atmospheric pressure, $Da = (u'/S_u^0)^{-1}(l_T/\delta_f)$ is the Damköhler number.

	Correlation	Equation	C_2H_4 MAPE (%)	NH_3/CH_4 MAPE (%)
C1	This work	$S_T/S_u^0 \sim Ge(1+Re_T)^{0.5}$ $Ge = {Re_T}^{0.5}[1-\exp(-(\delta_f/u')/t)]^{0.9}$	7.8	8.5
C2	Chaudhuri *et al.* [17].	$S_T/S_u^0 \sim Re_T^{0.5}$	18.1	13.9
C3	Cant *et al.* [43].	$S_T/u' \sim 0.5Re_T^{0.25}$	56.9	33.2
C4	Kobayashi [44]	$S_T/S_u^0 \sim 2.9(u'/S_u^0)^{0.38}(P/P_0)^{0.38}$	65.1	58.4
C5	Gülder [45]	$S_T/S_u^0 \sim 1+0.62(u'/S_u^0)^{0.5}Re_T^{0.25}$	65.2	55.4
C6	Anand & Pope [46]	$S_T/S_u^0 \sim 1.5u'/S_u^0$	67.2	39.2
C7	Zel'dovich *et al.* [47].	$S_T/S_u^0 \sim 1+(u'/S_u^0)(1+Da^{-2})^{-0.25}$	71.6	39.2
C8	Muppala *et al.* [48].	$S_T/S_u^0 \sim 1+0.46Le^{-1}Re_T^{0.25}(u'/S_u^0)^{0.3}(P/P_0)^{0.3}$	75.1	73.3
C9	Zimont [49]	$S_T/u' \sim 0.52Da^{0.25}$	76.2	76.2
C10	Liu *et al.* [50].	$S_T/S_u^0 \sim 1+0.14u'/S_u^0 Da^{0.47}$	80.7	82.3
C11	Ronney [51]	$S_T/S_u^0 \sim 1+0.12u'/S_u^0 Da^{0.5}$	81.4	83.5

It is found that, when $a = 0.5$, $b = 0.9$, i.e., the extended correlation with the form of

$$S_T/S_u^0 \sim Ge(1+Re_T)^{0.5}, \quad Ge = {Re_T}^{0.5}[1-\exp(-(\delta_f/u')/t)]^{0.9}, \tag{21}$$

has the minimal MAPE of 7.8% and 8.5% for ethylene/air and ammonia/methane/air flames, respectively. Evolution of the nondimensional prefactor Ge is shown in Figs. 11(a) and 11(b) for the two flames, respectively. As shown, the prefactor Ge decreases rapidly in the initial stage, then slowly, and approaches a constant value in the final stage with the magnitude of about unity. This suggests that geometry and history effects significantly influence the initial stage of flame propagation, but gradually diminish as the flame expands, and eventually vanish as the flame fully develops into a turbulent planar flame. The prefactor Ge approaches a constant value once the flame is fully developed, with this value determined by the initial conditions, such as fuel mixtures and pressures.

As the flame fully develops, the above correlation, Eq. (21), approaches

$$S_T/S_u^0 \sim 1+{Re_T}^{0.5} \tag{22}$$

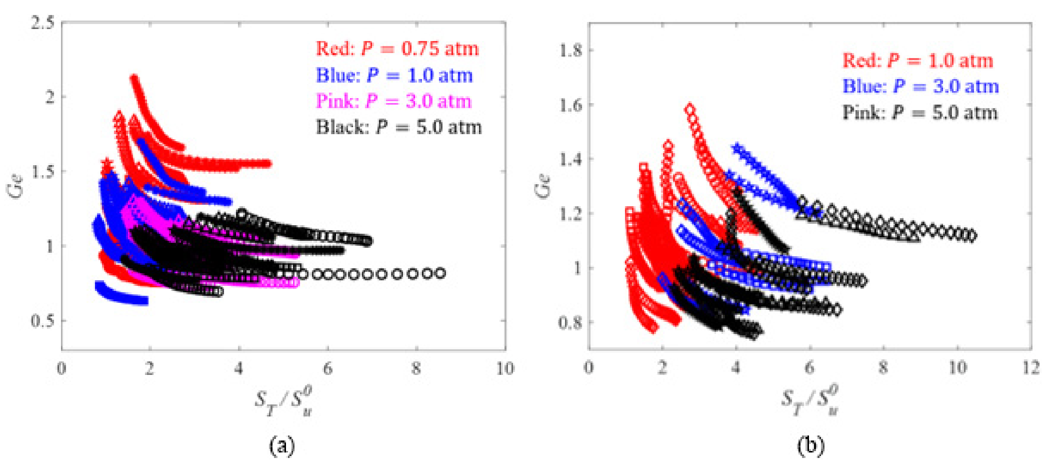

FIG. 11. Evolution of the nondimensional prefactor Ge. (a) Ethylene/air and (b) Ammonia/methane/air.

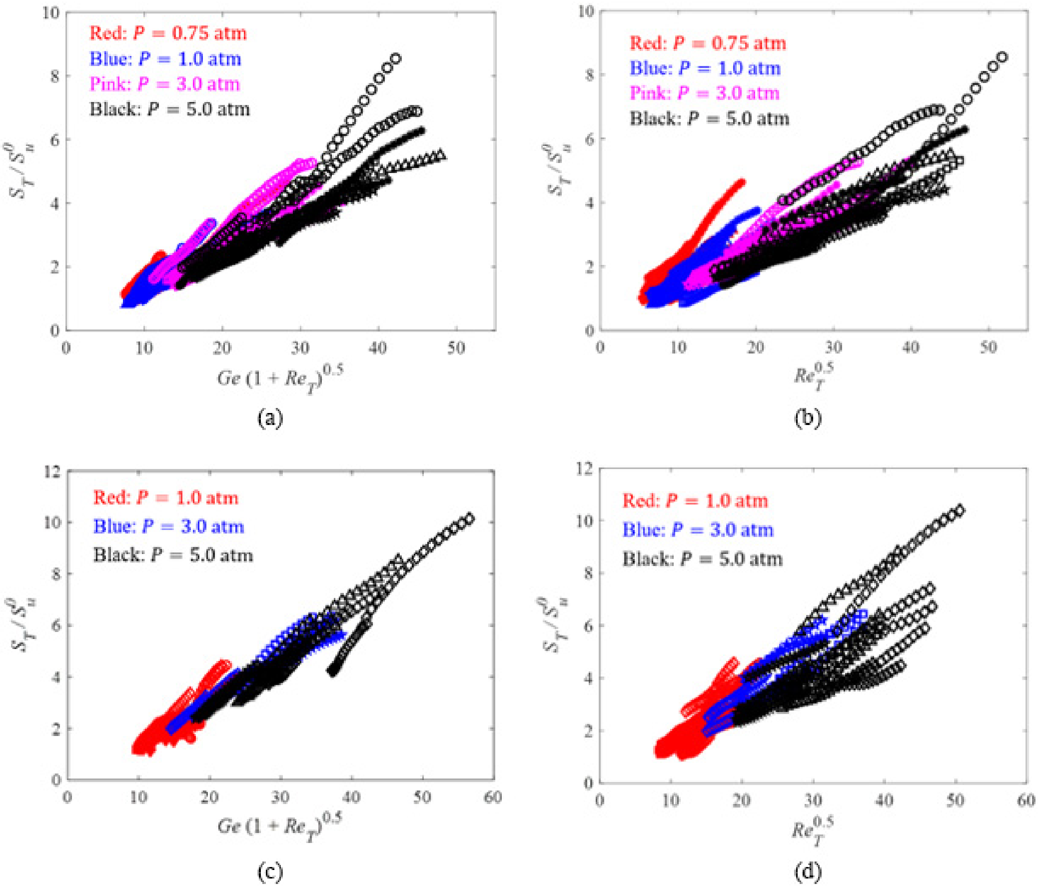

FIG. 12. Normalized turbulent flame speed verified by two correlations. The scaling correlation in (a), (c) is proposed in this work. The scaling correlation in (b), (d) is proposed by Chaudhuri *et al.* [17]. (a), (b) Ethylene and (c), (d) Ammonia/methane.

for the turbulent flame with a small Reynolds number, and

$$S_T/S_u^0 \sim {Re_T}^{0.5} \tag{23}$$

for the turbulent flame with a large Reynolds number, which is the same as the correlation proposed in Ref. [17]. Figure 12 shows the verification of the scaling correlation proposed in this work and in Ref. [17] for ethylene/air and ammonia/methane/air flames, respectively. The extended correlation exhibits stronger linearity and centrality, thereby improving the accuracy in predicting turbulent flame speeds. However, for methane/ammonia/air mixtures, a rounding value of $b = 0.9$ was used for simplification in the extended correlation, leading to a systematic deviation that results in a slightly higher MAPE compared to that of ethylene/air mixtures.

3. *Comparison among various scaling correlations*

Details of the correlations are summarized in Table VI for increasing MAPE of ethylene/air flames. The correlation has been validated for ethylene/air and ammonia/methane/air turbulent expanding flames, with mean absolute percentage errors (MAPE) of 7.8% and 8.5%, respectively. It is seen that both the correlations C1 (proposed in this work) and C2 (proposed in Ref. [17]) show relatively small MAPE compared to other correlations, while the extended correlation accounting for the geometry and history effects shows improved performance, and has the smallest MAPE among both complex and simple correlations listed in the table. To further validate its universality, future work will include experiments across a broader range of turbulent regimes for expanding flames. This will involve refining the time-dependent nondimensional factor to explicitly account for geometric effects via the flame-radius-based Reynolds number.

V. CONCLUDING REMARKS

In this study, a PIV system was used to calibrate the turbulent flow field within a constant-pressure expanding flame apparatus driven by eight symmetrical fans. Results show that the mean velocity and velocity fluctuation covariance are nearly zero across the field, with homogeneity and isotropy normalized by fluctuation velocity mostly within $\pm 20\%$. These results show that the turbulence is almost homogeneous and isotropic. The fluctuation velocity ranges from 0.70 m/s to 1.77 m/s with the fan rotation speed varying from 3000 rpm to 7000 rpm, while the integral length scale maintains about 10 mm for all cases.

The turbulent flame speeds are measured over a wide turbulent Reynolds number ($Re_T = u'R_f/S_u^0\delta_f$) range of $29 \sim 2706$ and $69 \sim 2560$ for ethylene/air and ammonia/methane/air flames, respectively. To characterize the propagation properties of turbulent flames, an extended scaling correlation for turbulent flame speed is proposed, which accounts for both geometry and history effects in flame propagation, i.e., $S_T/S_u^0 \sim Ge(1 + Re_T)^{0.5}$, $Ge = {Re_T}^{0.5}[1 - \exp(-(\delta_f/u')/t)]^{0.9}$.

In particular, this scaling approach differs from previous methods by incorporating a time-dependent nondimensional factor that also includes geometry effects through the flame-radius-based Reynolds number. The correlation has been validated for turbulent expanding flames of ethylene/air and ammonia/methane/air, with MAPE of 7.8% and 8.5%, respectively. This demonstrates relatively higher accuracy compared to other existing scaling correlations.

ACKNOWLEDGMENTS

The work at Tsinghua University was supported by the National Natural Science Foundation of China No. 52025062. We thank Dr. Minglei Li and Dr. Ning Wu for their contributions in the construction of the constant-pressure, dual-chambered, expanding flame apparatus.

---

[1] N. Peters, *Turbulent Combustion* (Cambridge University Press, Cambridge, 2000).
[2] G. Damköhler, Der einfluss der turbulenz auf die flammengeschwindigkeit in gasgemischen, **46**, 601 (1940).
[3] N. Peters, Laminar flamelet concepts in turbulent combustion, Symp. (Int.) Combust. **21**, 1231 (1988).
[4] K. N. C. Bray, The challenge of turbulent combustion, Symp. (Int.) Combust. **26**, 1 (1996).
[5] N. Peters, The turbulent burning velocity for large-scale and small-scale turbulence, J. Fluid Mech. **384**, 107 (1999).
[6] A. N. Lipatnikov and J. Chomiak, Turbulent flame speed and thickness: Phenomenology, evaluation, and application in multi-dimensional simulations, Prog. Energy Combust. Sci. **28**, 1 (2002).
[7] A. N. Lipatnikov and J. Chomiak, Molecular transport effects on turbulent flame propagation and structure, Prog. Energy Combust. Sci. **31**, 1 (2005).
[8] J. F. Driscoll, Turbulent premixed combustion: Flamelet structure and its effect on turbulent burning velocities, Prog. Energy Combust. Sci. **34**, 91 (2008).
[9] D. Bradley, M. Lawes, and M. S. Mansour, Flame surface densities during spherical turbulent flame explosions, Proc. Combust. Inst. **32**, 1587 (2009).
[10] P. Brequigny, F. Halter, and C. Mounaim-Rousselle, Lewis number and Markstein length effects on turbulent expanding flames in a spherical vessel, Exp. Therm. Fluid Sci. **73**, 33 (2016).

[11] J. Goulier, N. Chaumeix, F. Halter, N. Meynet, and A. Bentaib, Experimental study of laminar and turbulent flame speed of a spherical flame in a fan-stirred closed vessel for hydrogen safety application, Nucl. Eng. Des. **312**, 214 (2017).
[12] A. N. Lipatnikov, W. Y. Li, L. J. Jiang, and S. S. Shy, Does density ratio significantly affect turbulent flame speed, Flow Turbul. Combust. **98**, 1153 (2017).
[13] Z. Lu and Y. Yang, Modeling pressure effects on the turbulent burning velocity for lean hydrogen/air premixed combustion, Proc. Combust. Inst. **38**, 2901 (2020).
[14] E. M. Burke, F. Güthe, and R. F. D. Monaghan, in *Proceedings of ASME Turbo Expo*, Turbomachinery Technical Conference and Exposition (ASME, New York, 2016).
[15] R. Sankaran, E. R. Hawkes, J. H. Chen, T. Lu, and C. K. Law, Structure of a spatially developing turbulent lean methane/air Bunsen flame, Proc. Combust. Inst. **31**, 1291 (2007).
[16] J. B. Bell, M. S. Day, J. F. Grcar, M. J. Lijewski, J. F. Driscoll, and S. A. Filatyev, Numerical simulation of a laboratory-scale turbulent slot flame, Proc. Combust. Inst. **31**, 1299 (2007).
[17] S. Chaudhuri, F. J. Wu, D. L. Zhu, and C. K. Law, Flame speed and self-similar propagation of expanding turbulent premixed flames, Phys. Rev. Lett. **108**, 044503 (2012).
[18] E. C. Okafor, Y. Naito, S. Colson, A. Ichikawa, T. Kudo, A. Hayakawa, and H. Kobayashi, Measurement and modelling of the laminar burning velocity of methane-ammonia-air flames at high pressures using a reduced reaction mechanism, Combust. Flame **204**, 162 (2019).
[19] S. Li, S. Zhang, H. Zhou, and Z. Ren, Analysis of air-staged combustion of NH_3 /CH_4 mixture with low NOx emission at gas turbine conditions in model combustors, Fuel **237**, 50 (2019).
[20] E. C. Okafor, Y. Naito, S. Colson, A. Ichikawa, T. Kudo, A. Hayakawa, and H. Kobayashi, Experimental and numerical study of the laminar burning velocity of $CH_4 - NH_3$–air premixed flames, Combust. Flame **187**, 185 (2018).
[21] B. Meredith, and J. Spadaccini, Scramjet fuels autoignition study, J. Propuls. Power **17**, 315 (2001).
[22] T. Carriere, P. R. Westmoreland, A. Kazakov, Y. S. Stein, and F. L. Dryer, Modeling ethylene combustion from low to high pressure, Proc. Combust. Inst. **29**, 1257 (2002).
[23] D. A. Sheen, X. You, H. Wang, and T. Løvås, Spectral uncertainty quantification, propagation and optimization of a detailed kinetic model for ethylene combustion, Proc. Combust. Inst. **32**, 535 (2009).
[24] C. Xu and A. A. Konnov, Validation and analysis of detailed kinetic models for ethylene combustion, Energy **43**, 19 (2012).
[25] J. Huo, T. Shu, Z. Ren, and C. K. Law, Extrapolation of laminar ethylene/air flame speeds at elevated pressures with flame chemistry analysis, J. Propul. Power **35**, 424 (2018).
[26] C. S. Yoo, E. S. Richardson, R. Sankaran, and J. H. Chen, A DNS study on the stabilization mechanism of a turbulent lifted ethylene jet flame in highly-heated coflow, Proc. Combust. Inst. **33**, 1619 (2011).
[27] S. Golder, and J. J. Doom, in *55th AIAA Aerospace Sciences Meeting* (American Institute of Aeronautics and Astronautics, Reston, Va, 2017).
[28] P. R. Medwell, P. A. M. Kalt, and B. B. Dally, Imaging of diluted turbulent ethylene flames stabilized on a Jet in Hot Coflow (JHC) burner, Combust. Flame **152**, 100 (2008).
[29] J. Huo, S. Yang, Z. Ren, D. Zhu, and C. K. Law, Uncertainty reduction in laminar flame speed extrapolation for expanding spherical flames, Combust. Flame **189**, 155 (2018).
[30] T. Shu, Y. Xue, Z. Zhou, and Z. Ren, An experimental study of laminar ammonia/methane/air premixed flames using expanding spherical flames, Fuel **290**, 120003 (2021).
[31] S. Yang, A. Saha, Z. R. Liu, and C. K. Law, Role of Darrieus-Landau instability in propagation of expanding turbulent flames, J. Fluid Mech. **850**, 784 (2018).
[32] Z. Liu, S. Yang, C. K. Law, and A. Saha, Cellular instability in $Le < 1$ turbulent expanding flames, Proc. Combust. Inst. **37**, 2611 (2019).
[33] V. y. Akkerman, S. Chaudhuri, and C. K. Law, Accelerative propagation and explosion triggering by expanding turbulent premixed flames, Phys. Rev. E **87**, 023008 (2013).
[34] S. Chaudhuri, F. J. Wu, and C. K. Law, Scaling of turbulent flame speed for expanding flames with Markstein diffusion considerations, Phys. Rev. E **88**, 033005 (2013).
[35] S. Chaudhuri, A. Saha, and C. K. Law, On flame–turbulence interaction in constant-pressure expanding flames, Proc. Combust. Inst. **35**, 1331 (2015).

[36] A. A. Townsend, The measurment of double and triple correlation derivatives in isotropic turbulence, Math. Proc. Cambridge Philos. Soc. **43**, 560 (1947).

[37] S. B. Pope, *Turbulent Flows* (Cambridge University Press, Cambridge, 2000).

[38] USC Mech Version II. High-temperature combustion reaction model of H_2 /CO/C1-C4 compounds, http://ignis.usc.edu/USC_Mech_II.htm.

[39] J. Huo, A. Saha, T. Shu, Z. Ren, and C. Law, Self-acceleration and global pulsation in expanding laminar H_2-O_2-N_2 flames, Phys. Rev. Fluids **4**, 043201 (2019).

[40] S. Chaudhuri, V. y. Akkerman, and C. K. Law, Spectral formulation of turbulent flame speed with consideration of hydrodynamic instability, Phys. Rev. E **84**, 026322 (2011).

[41] P. Goix, P. Paranthoen, and M. Trinite, A tomographic study of measurements in a V-shaped H_2/air flame and a lagrangian interpretation of the turbulent flame brush evolution, Combust. Flame **81**, 229 (1990).

[42] B. Renou, A. Mura, E. Samson, and A. Boukhalfa, Characterization of the local flame structure and the flame surface density for freely propagating premixed flames at various Lewis numbers, Combust. Sci. Technol. **174**, 143 (2002).

[43] R. S. Cant, S. B. Pope, and K. N. C. Bray, Modelling of flamelet surface-to-volume ratio in turbulent premixed combustion, Symp. (Int.) Combust. **23**, 809 (1991).

[44] H. Kobayashi, Experimental study of high-pressure turbulent premixed flames, Exp. Therm Fluid Sci. **26**, 375 (2002).

[45] Ö. L. Gülder, Turbulent premixed flame propagation models for different combustion regimes, Symp. (Int.) Combust. **23**, 743 (1991).

[46] M. S. Anand and S. B. Pope, Calculations of premixed turbulent flames by PDF methods, Combust. Flame **67**, 127 (1987).

[47] I. B. Zel'dovich, G. I. Barenblatt, V. B. Librovich, and G. M. Makhviladze, *Mathematical Theory of Combustion and Explosions* (Springer, New York, 1985).

[48] S. P. R. Muppala, N. K. Aluri, F. Dinkelacker, and A. Leipertz, Development of an algebraic reaction rate closure for the numerical calculation of turbulent premixed methane, ethylene, and propane/air flames for pressures up to 1.0 MPa, Combust. Flame **140**, 257 (2005).

[49] V. L. Zimont, Gas premixed combustion at high turbulence. Turbulent flame closure combustion model, Exp. Therm Fluid Sci. **21**, 179 (2000).

[50] C. C. Liu, S. S. Shy, M. W. Peng, C. W. Chiu, and Y. C. Dong, High-pressure burning velocities measurements for centrally-ignited premixed methane/air flames interacting with intense near-isotropic turbulence at constant Reynolds numbers, Combust. Flame **159**, 2608 (2012).

[51] P. D. Ronney, *Some Open Issues in Premixed Turbulent Combustion* (Springer, Berlin, 1995).